First principles calculations on CeO_2 doped with Tb^{3+} ions

Andrew Chesnokov[a], Denis Gryaznov[a], Eugene Kotomin[a,b]

[a]Institute of Solid State Physics, University of Latvia, Kengaraga 8, Riga LV-1063, Latvia
[b]Max Planck Institute for Solid State Research, Heisenbergstr. 1, Stuttgart D-70569, Germany

Abstract. The atomic and electronic structure of CeO_2 doped with Tb has been calculated from first principles with inclusion of strong correlation effects on the basis of Hubbard model (GGA+U). The two values of Hubbard U-parameter were applied separately on Ce and Tb ions, in order to treat correctly two oxidation states of Tb (3+ and 4+). Crystal structure distortion is also discussed for Tb3+ ions in ceria without oxygen vacancies. The corresponding total energy difference between the 3+ and 4+ states is very small and, thus, these states can co-exist without oxygen vacancy formation (unlike Gd doping). Multiple configurations have been obtained with localization of electrons on different number of cations, if the Tb ion has an oxygen vacancy nearby. A site symmetry approach has been successfully applied to identify the ground state configuration. Gibbs formation energy of oxygen vacancy due to Tb doping is reduced by almost a factor of four, in comparison with the pure CeO_2. The dependence of Gibbs formation energy on the temperature and oxygen partial pressure is discussed. It has been also shown that the lowest formation energy for the small polaron occurs when the Ce^{3+} and Tb^{3+} ions are located as nearest neighbors to oxygen vacancy. The results obtained are compared with the existing literature data from the electrical conductivity and optical measurements.

1. Introduction

CeO_2 (ceria) continues to attract great interest due to its numerous applications, such as electrolyte for solid oxide fuel cells and oxygen separation membranes (high ionic conductivity) [1], electromechanics (high electrostriction coefficient) [2] and catalysis [3]. These properties are improved upon CeO_2 doping with the lanthanide ions. For example, Gd- and Tb-doped CeO_2 demonstrates higher electrical conductivity in comparison with the undoped samples [4,5]. The Gd impurity is always present in the oxidation state 3+ and thus is compensated by formation of positively charged oxygen vacancies. In contrast, the Tb impurity can be in both 3+ and 4+ oxidation states and charge compensation by oxygen vacancies is not here so obvious. Another difference is that the Gd^{3+} shows a limited solubility in ceria [6] unlike unlimited solubility of Tb^{4+} [7]. Large electronic conductivity due to a mixed valence state of Tb impurity makes enhanced ceria performance in mixed conductive membranes for oxygen separation [8,9].

Generally, oxygen vacancies (V_O) play significant role in Tb-doped CeO_2. Their role was discussed in detail not only for higher electrical conductivities in $Ce_{1-x}Tb_xO_{2-\delta}$ (where x varies from 0.1 to 0.5) [5] but also for their control of optical properties in Tb-doped nanocrystalline CeO_2 (1-10% mol [10] and 5% mol [11]). Upon Tb 3+ doping higher VO concentration arises resulting in the lattice strain [10]. According to optical measurements [11], V_O could be responsible for the visible light emission (~2.5 eV). Density functional calculations are helpful for better understanding of Vo behavior in oxides which has been demonstrated in numerous studies (e.g., [12,13]). Moreover, oxygen vacancies create small polarons with several possible configurations. Recently, we suggested a site symmetry approach for their identification in undoped CeO2 [14]. In the present study, we used the same approach in calculations of the V_O's properties and behavior of holes in Tb-doped CeO_2.

In Section 2 we discuss computation details. Main results and discussion are presented in Section 3 which is sub-divided into two parts: comparison of Tb^{3+} and Tb^{4+} behavior in CeO_2 without vacancies in Section 3.1 and simultaneous presence of Tb and Vo in Section 3.2. In Section 4 main conclusions are summarized.

2. Computational details

We use the VASP 5.3 [15–17] computer code with the projector augmented wave method and the scalar relativistic pseudopotentials [15] with 12 valence electrons on Ce, 19 electrons on Tb, and 6 electrons on O atoms. The exchange-correlation functional was that due to Perdew, Becke and Ernzerhof (PBE) [18]. We employ the rotationally-invariant Dudarev's form of the so-called GGA+U_{eff} approach [19] as implemented in the VASP code. The two values of the Hubbard U_{eff}-parameter (hereafter, U) were fixed at 4f-orbitals of Ce and Tb atoms separately, in accordance with the literature data, i.e. 5.0 [20,21] and 6.0 [22] eV, respectively. It should be emphasized that we do not consider a hole trapping effects on O ions and, thus, do not apply the U-parameter to O 2p electrons [20]. The cut-off energy was fixed at 520 eV throughout all the spin-polarized calculations with the full atomic and electronic structure optimization. We use the supercell model of defective CeO_2 with impurity Tb atom and oxygen vacancy (V_O) present simultaneously.

CeO_2 possess a fluorite structure (space group $Fm\bar{3}m$, face-centered cubic lattice). In the present calculations, the supercell was constructed from the primitive unit cell using the non-diagonal expansion of lattice vectors, namely $(-2\ \ 2\ \ 2)$, $(2\ \ -2\ \ 2)$, $(2\ \ 2\ \ -2)$. It leads to the commonly used supercell consisting of 96 atoms, i.e. of 32 primitive unit cells. One Tb atom is introduced on the Ce sub-lattice corresponding to defect concentration of ~3%. Recently, we have demonstrated importance of site symmetry approach [23–25] and group-theoretical analysis for the calculations of defects in oxides [26,27] and, in particular, polaron properties in CeO_2 [14]. It was demonstrated in [14] that in the 96-atom supercell 64 oxygen atoms therein are split into two orbits, with symmetry C_{1h} (=C_s) and C_{3v}, whereas the 32 Ce atoms are split into three orbits, namely O_h, D_{4h}, and C_{2v}. Interested reader could refer to fig. S1 in Supplementary Information where the oxygen and cerium sublattices are depicted with corresponding site symmetry positions. It was also concluded that for undoped CeO_2 containing V_O, the symmetry point group C_s or C_{2v} is suitable for the formation of a small polaron, with two electrons of missing O^{2-} ion localized on the two nearest Ce^{3+} ions.

Here we use the same approach to analyze the effect of Tb and the formation of polarons. In the present study, all the calculations with V_O in the supercell were performed for the C_s and C_{2v} symmetry point groups, if not otherwise stated. Moreover, the effects of symmetry reduction for Tb without V_O were also considered and required the considerations of with O_h, D_{4h}, and C_{2v} symmetry point groups for the Tb positions in the supercell (fig. S1). The integration in the reciprocal space over the Brillouin zone was performed using 2x2x2 Mokhorst-Pack mesh [28].

The Gibbs formation energy of Vo in the Tb doped CeO_2 was calculated as

$$\Delta G_F^{V_o} = E_{tot}^{Tb,V_o} - E_{tot}^{Tb} + \mu_O(T, p_{O_2}), \quad (1)$$

where E_{tot}^{Tb,V_o}, E_{tot}^{Tb} the total electronic energy of supercell containing both Tb and V_O simultaneously and that without V_O, respectively. The oxygen chemical potential $\mu_o(T, p_{O_2})$ was obtained following [29] and successfully applied in previous works [30–32]. Thus, the oxygen chemical potential $\mu_o(T, p_{O_2})$ is cast as

$$\mu_O(T, p_{O_2}) = \mu_O^0(T) + \frac{1}{2}k_B T\, ln\frac{p_{O_2}}{p^o} = E_{tot}^{AO} - E_{tot}^{A} - \Delta G^{AO}(T^0) + \Delta\mu_O(T) + \frac{1}{2}k_B T\, ln\frac{p_{O_2}}{p^0}, \quad (2)$$

where $\mu_O^0(T)$ $\mu_O^0(T)$ is the standard chemical potential, superscripts AO and A stand for the reference binary oxide, and its metal, respectively, and $\Delta G^{AO}(T^0)$ the standard heat formation of a binary oxide taken from the experimental database [33]. Thus, this approach has the advantage of avoiding the calculation of total energy of O_2 and suggests a connection with the experimental oxide of formation. $\Delta\mu_O(T)$ is the difference in chemical potential at the temperature of interest T and the standard state (T^0 = 298.15 K), which is also taken from the experimental database, k_B Boltzmann's constant, p_{O_2} and p^0 the oxygen partial pressure and standard pressure, respectively. In order to calculate $\mu_O(T, p_{O_2})$ we have treated several binary oxides and taken their average contribution. All the calculations of binary oxides included van der Waals interactions within the DFT+D3 approach suggested by Grimme et al. [34] in order to accurately reproduce the lattice parameters. In Supplementary Information (table S1) the calculated lattice parameters with and without van der Waals interactions for a comparison are given. In fig. 2 the dependence $\mu_O(T, p_{O_2})$ as calculated using Eq. 2 is shown. Notice that we neglected the vibrational contribution in the solid phase to the formation energy as irrelevant for the present study.

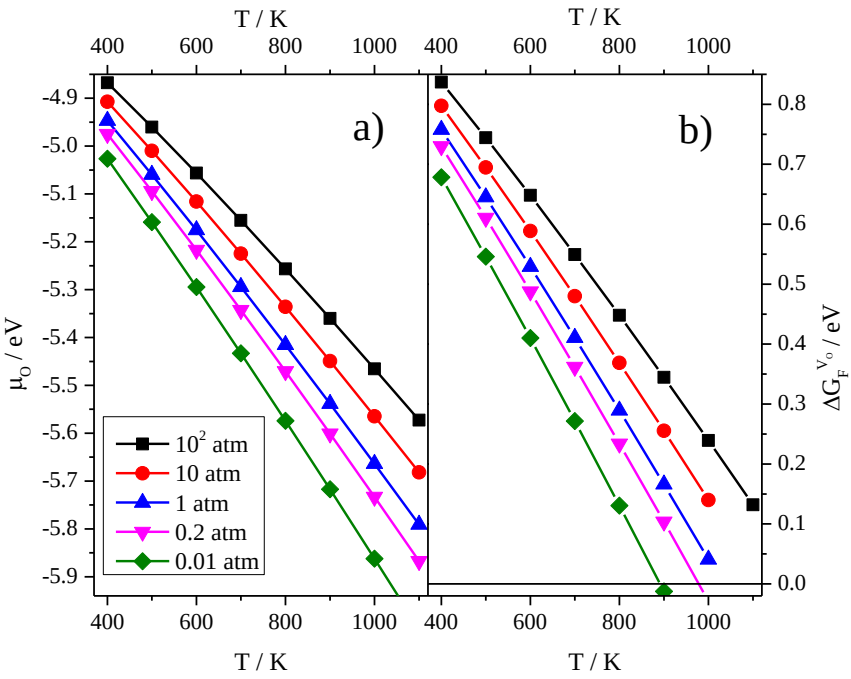

Fig. 1. The oxygen chemical potential due to Eq. 2 calculated in VASP a) and formation energy of oxygen vacancy due to Eq. 1 b) as a function of temperature (temperature range 400 – 1100 °K) and oxygen partial pressure (p_{O_2}).

3. Results and discussion

3.1. A comparison of parent oxides and delocalization of holes

We calculated atomic and electronic structure of Tb ions in the two oxidation states, 3+ and 4+, using neutral supercells without V_O's as the Tb ion is known to exist in a mixed valence state. We have considered all three Wyckoff positions for Tb substituting for Ce in the 96-atom supercell. All ions surrounding Tb in a given position were allowed to relax to

the minimum of total energy. In general, the Tb ion prefers to be in the 4+ oxidation state which follows from the total electronic energies difference of Tb^{3+} and Tb^{4+} (discussed below). These two oxidation states are identified by the calculated magnetic moments (μ) and the Tb-O bond lengths (table 1). In the 4+ state, the μ-value of Tb ion is 6.26 μ_B, which is close to 6.21 μ_B for Tb^{4+} in TbO_2 (also calculated in the present study). Also, the Tb-O bond length for Tb^{4+} in CeO_2 is only slightly larger than that in TbO_2, i.e. 2.32 vs 2.37 Å. The covalent effects are evident here as the formal μ of Tb^{4+} should be 7 μ_B. Reduction of symmetry did not lead to significant changes in the properties of Tb^{4+}. On the other hand, Tb_2O_3 (calculated in the present study in the bixbyite structure, table 1, the oxidation state of Tb is 3+) has two very close μ's of Tb ions around 5.99 μ_B dictated by symmetry. Despite close values of μ's the bond lengths of the two Tb ions in Tb_2O_3 are quite different. Besides, one of the two Tb ions occupies a low symmetrical C_{2h}-position and has three different distances to the closest O ions. Nevertheless, the μ-value of Tb^{3+} in CeO_2 is around 6 μ_B, too, and the Tb-O bond length is again slightly larger in comparison with Tb_2O_3. Importantly, a comparison with the parent oxides confirms the possibility to calculate the Tb ion in the 3+ oxidation state, provided the supercell symmetry is reduced down to the point group symmetry C_{2v}.

So, the total energy difference between the two Tb oxidation states at the C_{2v}-position is only 0.07 eV per supercell, in the favor of 4+ oxidation state. Even though the 4+ state is still more favorable, the two states could co-exist (a mixed valence state) in a real material under realistic conditions. This is consistent with the experimental lattice parameter dependences on Tb concentration [5] lying exactly between the two theoretical dependences for Tb^{4+} and Tb^{3+} estimated separately. In contrast, the cubic symmetry of the supercell restored with the Tb ion at O_h-position (fig. S1) is not sufficient for treatment of the 3+ oxidation state leading to unphysical results with too large μ-values for the Tb ions.

Clearly, the Tb^{3+} ion in the neutral supercell has to be compensated by an electronic hole. In our calculations the holes were obviously delocalized over a whole supercell, irrespective to any local structural distortions around the defect. One could expect intuitively holes localized on O ions nearest to the cation what happens often for the hole polarons in oxides, e.g. MgO:Li [35] and perovskites [13,36]. In addition, analysis of the electronic density of states (DOS) for $(Ce,Tb)O_2$ (fig. 1) and parent oxides TbO_2, Tb_2O_3 (fig. S2) could be helpful for interpretation of the differences between the two oxidation states.

Table 1. The magnetic moments of Tb in the two oxidation states (3+ and 4+) and corresponding Tb-O bond lengths depending on local site symmetry. The primitive unit cells of TbO_2 and Tb_2O_3 were of fluorite structure (space group Fm3m, face-centered cubic lattice) and bixbyite structure (C-type, space group $Ia\bar{3}$, N°206), respectively, calculated within the PBE+U_{eff} approach with the U_{eff} = 6.0 eV. The calculated lattice parameters were 5.35 and 10.70 Å for TbO_2 and Tb_2O_3, respectively. In the bixbyite structure Tb ions occupy two Wyckoff positions, namely Tb1 : 8b (coordinates ¼, ¼, ¼, point group symmetry S_6) and Tb2: 24d (coordinates -0.03171, 0, ¼, point group symmetry C_{2h}), leading, thus, to several values for the Tb magnetic moment μ and Tb-O bond length. Each Tb ion is surrounded by 6 oxygen ions in the bixbyite structure. In the case of low symmetrical position (24d) the 6 oxygen ions are split in pairs to form 3 Tb-O bonds.

Ion / System /Symmetry	μ(Tb) / μ_B	Bond length / Å
Tb^{4+}/ TbO_2/O_h	6.21	2.32
Tb^{4+}/$(Ce,Tb)O_2$/ O_h	6.21	2.37
Tb^{4+}/ $(Ce,Tb)O_2$/ C_{2v}	6.21*	2.37*
Tb^{3+}/ $(Ce,Tb)O_2$/ C_{2v}	6.08*	2.39, 2.40
Tb^{3+} /Tb_2O_3 / S_6, C_{2h}	5.99*	Tb1: 2.30, Tb2: 2.27, 2.29, 2.36

*Very close values of the property were obtained for all Tb ions in the supercell even though Tb site symmetry is low.

Fig. 2 shows an empty Ce 4f band in-between O 2p valence band and Ce 5d conduction band, thus, leading to two band gaps as in a pure CeO_2 [37,38]. The valence band is formed by O 2p electrons hybridized with Tb 4f electrons. Thus, the O 2p - Ce 4f band gap is ~2.1 eV in our calculations for Tb doped CeO_2 independently of the oxidation state. This value is slightly smaller than in the case of previous DFT+U calculations of undoped CeO_2 [39,40]. In addition, there is also an empty Tb 4f band above the Ce 4f band in the spin down states (fig. 1). This band is characterized by two intensive peaks whose positions depend slightly on the oxidation state. In the DFT+U calculations with the FP-(L)APW method for TbO_2 [22] this band was much closer to the valence band top suggesting a very small gap. However, the main counterparts in the calculated DOS are due to two occupied Tb 4f bands: a deep **band1** from -6.50 to -5.25 eV (consisting of two peaks in fig. 2a) in the spin up for the 3+ state (it is one peak from -6.5 to -6.0 eV for the 4+ state in fig. 2b) and **band2** in the spin down channel from -1.60 eV to 0.00 for the 3+ state (it is a broader band from -2.50 to 0.00 for the 4+ state). Notice that the presence of holes in the system is associated, in the Tb3+ case, with increased density of O 2p states at the Fermi energy. In fig. S2 the DOS around the Fermi energy for both Tb3+ and Tb4+ in CeO2 is shown for clarity. One could also see that the Fermi energy is considerably occupied in TbO2 whereas it is unoccupied in Tb2O3 (fig. S3). Actually, the occupation of Fermi energy by O 2p states is even more pronounced for an increased Tb concentration in CeO2 [7]. In the electrical conductivity measurements [5] the p-type conductivity was identified at Tb concentration around 50% .Tb_2O_3 has an additional **band3** at -4.25 eV (fig. S2). It explains the appearance of three peaks in the range -6.0-4.0 eV for the 3+ state in fig. 2a. It is worth mentioning that the two peaks were also observed in the GW_0 calculations with the FP-(L)APW method for Tb_2O_3 [41]. However, our calculated **band1** and **band3** for Tb_2O_3 are shifted to deeper energies in comparison with these calculations. As seen, **band2** is strongly hybridized with the O 2p electrons. Notice that the effect of O2p-4f hybridization was earlier evidenced in the XAS measurements of Karnatak et al. [42]. It is interesting to mention that the position of **band1** for TbO_2 is much deeper in (L)APW calculations [22]. We suggest that the difference between our results and those in [22] arises due to a more ionic picture for TbO_2 in the latter study which is reflected in their calculated magnetic moment of Tb being almost 7 μ_B.

a)

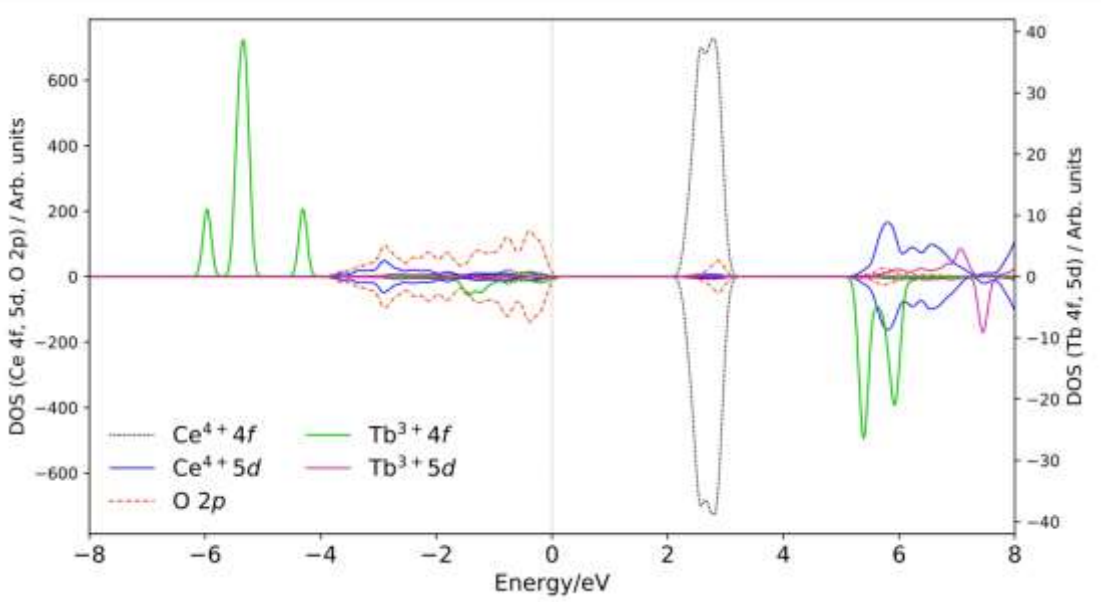

b)

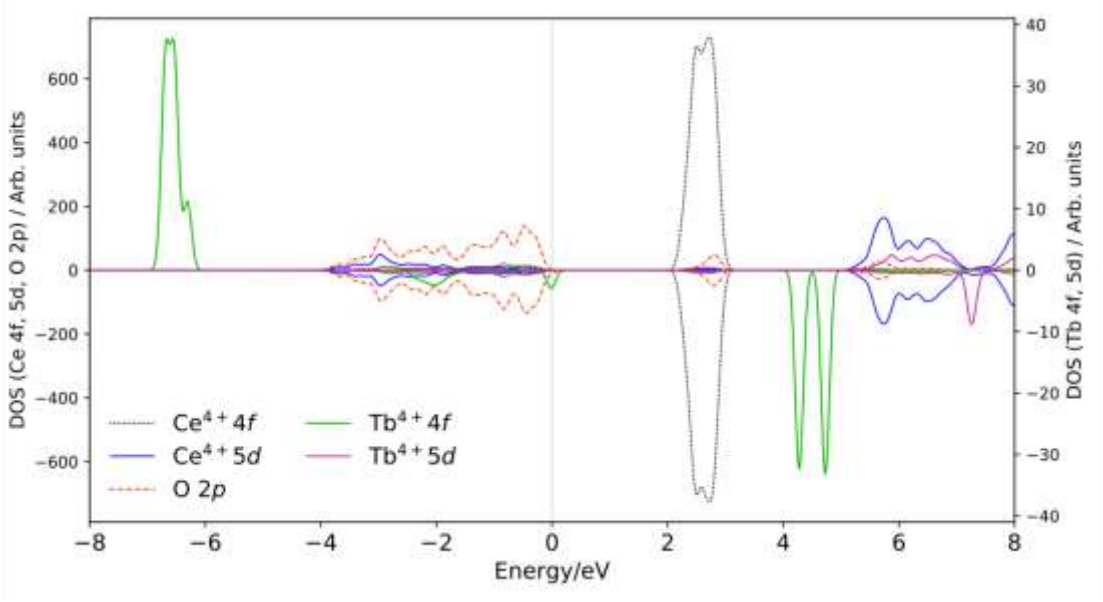

Fig. 2. The electronic density of states (DOS in arb. units) for a) Tb^{3+} and b) Tb^{4+} at the C_{2v} position in CeO_2.The Fermi energy is taken for zero.

3.2. Tb^{3+} ions near oxygen vacancies. Formation of small polarons

As is well known, the electronic conductivity in undoped CeO_2 arises due to the small polaron hopping over Ce^{3+} ions, as demonstrated both theoretically [14,40,43] and experimentally [44,45]. The Ce^{4+} ion reduction happens due to an electron transfer from nearest missing oxygen atom (formation of V_O). We have demonstrated in recent calculations [14] that several possible charge and spin redistributions (small and large radius polarons) differ considerably in energy. In the present calculations, V_O was modelled similarly, by removing a single oxygen ion from the 96-atom supercell, containing now one Tb ion (V_O concentration ~3%). From the symmetry viewpoint, V_O has occupied either C_s or C_{3v} position (fig. S1b) at the distance 2.34 Å from the Tb ion (first nearest neighbor) in the O_h

position, before the full structure relaxation. In this Tb position, its nearest neighbors are 8 O ions at the C_{3v} positions whereas each O ion in the supercell has 4 nearest cations.

We consider first two cases: several configurations when V_O is the first nearest neighbor of Tb and/or Ce (three configurations in table 2 and four configurations in table 3) and only one configuration when Vo is third nearest neighbor of both Tb and Ce (table 2). The only difference between the results in table 2 and table 3 is in the degree of localization. I.e., the two electrons left from the missing oxygen ion are localized on 4f orbitals of neighboring lanthanide cations. Evarestov *et al*. [14] observed in undoped ceria different possible polaron configurations with electron localization on one, two, three, or all four nearest Ce cations (first nearest neighbors). The configurations are characterized by the value of spin projection S_z due to localization on different number of cations. It was demonstrated that localization of two electrons on 4f orbitals of two nearest Ce cations corresponding to formation of a small polaron is energetically the most favorable case, about 0.61 eV lower in energy than the large radius polaron with localization on all four Ce ions. So, the minimum energy state was observed for S_z = 1 at low symmetrical C_s(or, alternatively, at C_{2v})-position of V_O in the 81-atom supercell.

Table 2. Formation of one Ce^{3+} and one Tb^{3+} near V_o. d(Tb^{3+}(Ce^{3+})-V_O) the distance between the Tb^{3+}(Ce^{3+}) ion and V_O before the structure optimization estimated from unrelaxed fluorite structure with the lattice constant 5.41 Å. d(Tb^{3+}-Ce^{3+}) the distance between the Tb^{3+} ion and Ce^{3+} ion after the full structure optimization. $\Delta G_F^{V_o}$ the Gibbs formation energy of V_o calculated with respect to the chemical potential of oxygen μ_O at T= 400 K and p=p^0 (fig. 1). All configurations are for the spin projection S_z = 1 and anti-ferromagnetic (AFM) spin alignment.

d(Tb^{3+}-V_O)/ Å	d(Ce^{3+}-V_O) /Å	d(Tb^{3+}-Ce^{3+})/ Å	μ(Tb^{3+}) / μ_B	q(Tb^{3+})/ e	μ(Ce^{3+})/ μ_B	q(Ce^{3+})/ e	$\Delta G_F^{V_o}$ / eV
2.34	2.34	4.13	6.03	2.09	-0.93	2.09	1.20
2.34	4.59	6.76	6.06	2.09	-0.93	2.13	0.70
4.49	2.34	6.76	6.05	2.12	-0.88	2.12	1.08
4.49	4.49	7.79	6.05	2.12	-0.97	2.14	0.99

Table 3. The electron density localization on Tb and Ce ions nearest to vacancy. Solutions with different spin projection S_Z. d(Tb^{3+}-Ce^{3+}) the distance between the Tb^{3+} ion and Ce^{3+} ion after the structure optimization. $\Delta G_F^{V_o}$ the Vo formation energy calculated with respect to the chemical potential of oxygen at T= 400 K and p_{O_2}=p^0. The distances between Ce^{3+}(Tb^{3+}) and Vo is 2.34 Å before the structure optimization estimated from unrelaxed fluorite structure with the lattice constant 5.41 Å. All the calculations were performed with the C_{3v} point group symmetry.

S_z	d(Tb^{3+}-Ce^{3+})/ Å	μ(Tb^{3+})/ μ_B	q(Tb^{3+})/ e	μ(Ce^{3+})/ μ_B	q(Ce^{3+})/ e	$\Delta G_F^{V_o}$ / eV
-1	3x4.18	6.07	2.08	3 x -0.35	2.32	1.32
2	4.17	6.04	2.08	3 x 0.37	2.30	1.14
1/2	0	6.05	2.09	-	-	1.52
3/2	4.18	6.25	2.17	3 x 0.71	2.22	2.61

In contrast to undoped system, a combination of Tb impurity and V_O in the same supercell leads to a more complex situation, as the distance between the Tb and V_O should

play a role. In Table 2 we collected results with respect to the spin projection S_z = 1, AFM spin alignment, cation-V_O distance and electron localization on two cations only whereas configurations with localization on larger number of cations are collected in table 3. The configurations in table 2 show a significant variation in $\Delta G_F^{V_o}$, from 0.70 to 1.20 eV. The Tb and Ce ions are always reduced due to the presence of V_O in the lattice. The μ-value of Tb ion in all configurations in table 2 is similar to that for Tb^{3+} in Tb_2O_3 (as discussed above). Therefore, one of the two electrons occupies the Tb 4f orbital whereas the second electron occupies the Ce 4f orbital meaning localization on two cations. The cation-V_O distances (d(Ce^{3+}-Vo) and d(Tb^{3+}-Vo)) are given before the atomic structure relaxation due to significant symmetry reduction and, consequently, difficult determination of such distances after the atomic structure relaxation.

As also seen in table 2, $\Delta G_F^{V_o}$ are reduced by almost a factor of 4, in a comparison with the undoped system ($\Delta G_F^{V_o}$= 2.68 eV in the present PBE+U_{eff} calculations at 400 K and p = p^0 vs 4.10 eV obtained with the hybrid PBE0 exchange-correlation functional [14]). The most energetically favorable case with $\Delta G_F^{V_o}$= 0.70 eV is characterized by the longer distance d(Ce^{3+}-V_o) of 4.59 Å (third nearest neighbor) whereas the configuration with $\Delta G_F^{V_o}$ of 1.20 eV – by the shortest distance d(Ce^{3+}-V_o) of 2.34 Å. Thus, the Tb^{3+} ion prefers to be the V_o first nearest neighbor whereas the Ce^{3+} cation – the *third* nearest neighbor in the configuration with the smallest $\Delta G_F^{V_o}$.

The main characteristics for Tb^{3+} (the presence of band1, band2, band3) in the calculated DOS are very similar to those discussed in fig. 1. The presence of Tb^{3+} in the band gap was not observed which is consistent with and is explained by $p_{O_2}^{-1/6}$ dependence of electrical conductivity [5] at low Tb content. As expected, the reduced Ce^{3+} cations induce a new peak in the band gap (fig. 2). This is an electron trap induced by V_o, located at ~1.0 eV below the bottom of unoccupied Ce 4f band (the O 2p — Ce 4f band gap is 2.1 eV). Recombination of trapped electrons with holes in the valence band could explain observation of a strong increase of the CeO_2 nanoparticle luminescence upon doping with Tb [11].

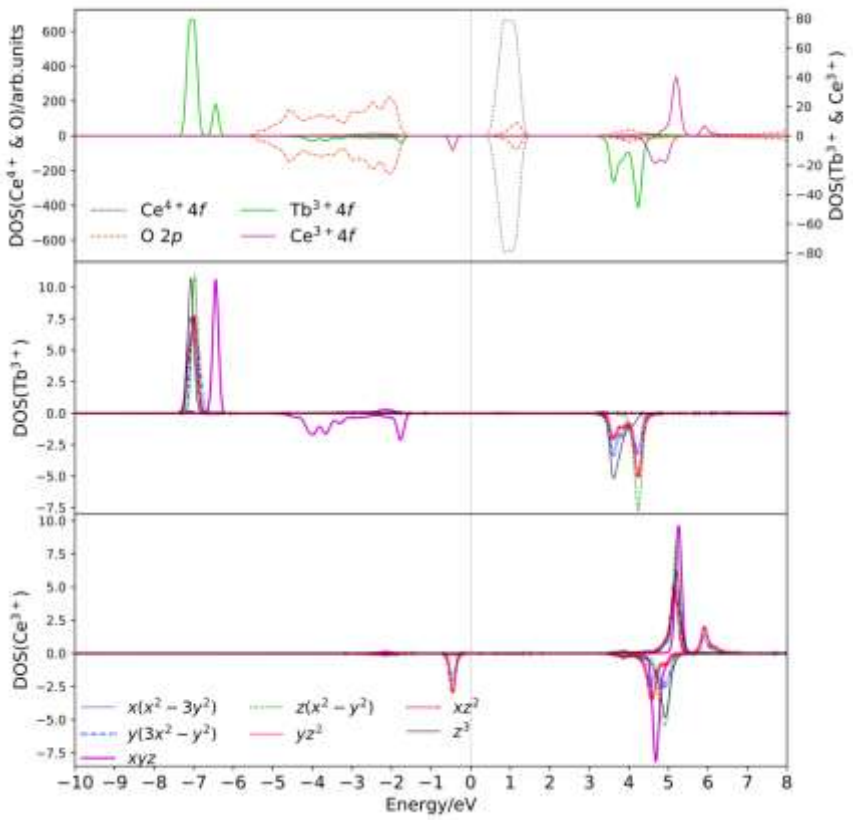

Fig. 3. DOS projected on 4f orbitals of Tb^{3+}, Ce^{3+}, Ce^{4+} and 2p orbitals of O, and its decomposition into all contributions from the 4f orbitals for two electrons from a missing oxygen atom localized on two cations (Ce and Tb, case with = 1.02 eV in table 1). Fermi energy is taken as zero.

The obtained results are qualitatively similar to the small polaron behavior in $SrTiO_3$. It was suggested for $SrTiO_3$ that the structure of the defect upon formation of V_o can be described as Ti^{3+}-Vo-Ti^{3+} [12]. I.e. the Ti^{3+} ions are considered as small polarons giving rise to emission band at 2.0 eV in the energy diagram. However, at the same time possible mechanisms may include recombination with the trapped holes which is responsible for the emission band at 2.8 eV. The optical measurements on Tb^{3+} in CeO_2 and $LaWO_6$ show the band at 498 nm (2.49 eV) [11], 544 nm (2.28 eV) [10] and 543 nm (2.28 eV) [46] in the emission spectra, respectively. Wang et al. related its presence to V_o and recombination with holes. Actually, the experiments in [11] included two dopants Eu^{3+} and Tb^{3+} which showed very similar behavior, and it was concluded that the emission band is not due to an impurity ion. In the same experimental considerations the excitation band was 426 nm (2.93 eV) [11], 381 nm (3.26 eV) [10]and 380 nm (3.26 eV) [46].

In fig. 3 the spin density maps are presented for two cases: two electrons from a missing oxygen ion localized on two (a) or four (b) cations. It clearly shows the effect of localized electrons on 4f orbitals of Tb^{3+} and Ce^{3+} ions. Such density maps are well comparable with the detailed DOS projected on all the 4f electron states (only effect of localization on two cations is shown in fig. 3). According to the density maps, and DOS for Tb^{3+} the second peak in **band 1** consists of $4f_{xyz}$ orbital whereas the first peak is formed of $4f_{z^3}$, $4f_{yz^3}$and $4f_{z(x^2-y^2)}$orbitals. Interestingly, **band 2** is also related to $4f_{xyz}$orbital. It could explain a nearly spherical shape of the spin density distribution for Tb^{3+} in contrast to

"flower" distribution for Ce^{3+}. The occupied Ce^{3+} band at 1.0 eV below the empty Ce^{4+} 4f band is formed by $4f_{yz^3}$, $4f_{xz^2}$ orbitals.

We treated also more complicated cases when two electrons from a missing oxygen ion were localized on the 4f orbitals of larger number of cations. Namely, the calculated configurations in table 3 show changes in $\Delta G_F^{V_o}$ and other properties in the cases of two electrons spread over three and four cations. Here the obtained configurations depend on the local site symmetry, too. The position of Tb was chosen O_h as was also done for the configurations in table 2. As we demonstrated [14], the C_{3v} point group is characterized by 4 configurations with the spin projection S_z= ½ (one electron localized on one cation only), 1 (one electron spread over 4 cations, AFM case), 3/2 (one electron spread over 3 cations, 2 (one electron spread over 4 cations, FM case). The most energetically unfavorable case with $\Delta G_F^{V_o}$ = 2.61 eV (table 3) is the one with Tb^{4+} in the supercell (and that is irrespective of Tb and V_o being first nearest neighbors), i.e. the two electrons are localized on three Ce ions in this configuration. The second unfavorable case ($\Delta G_F^{V_o}$= 1.52 eV) was obtained with the localization of one of the two electrons on Tb ion whereas the other electron is delocalized. So, localization on four cations is energetically more favorable than localization on Tb ion only or on three Ce ions.

In Supplementary Information we present also table 2 with additional configurations that confirm our main conclusions on the most stable configuration with localization on two cations with Tb being first nearest neighbor, and, it is more favorable to localize on four cations rather than on Tb ion only or three Ce ions.

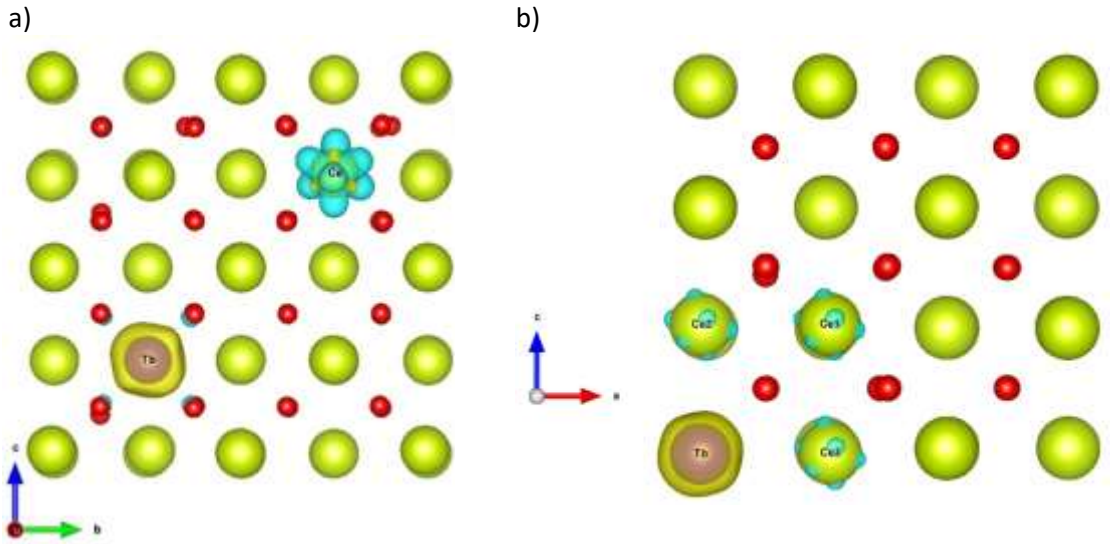

Fig. 4. Spin density maps for two electrons from a missing oxygen atom (a) localized on two cations (Tb and one Ce, $\Delta G_F^{V_o}$= 0.70 eV in table 2) or (b) four cations (Tb and three Ce, $\Delta G_F^{V_o}$= 1.32 eV in table 3). Bright yellow balls Ce ions, red balls O ions, brown ball Tb ion. Blue color denotes magnetic density on Ce ions whereas dark yellow color denotes magnetic density on Tb ion. Different colors of spin density on Tb and Ce cations are due to opposite spin alignment, corresponding to AFM solutions in table 2 and 3. The figure was drawn using the VESTA code [47].

Conclusions

It was demonstrated that the PBE+U_{eff} approach allows us to effectively consider localization of electronic defects and, thus, describe reduced cations in (Ce,Tb)O_2, i.e. Tb^{3+} and/or Ce^{3+}, in particular. We combined the PBE+U_{eff} calculations with the site symmetry approach to identify a necessary lattice distortion for the presence of Tb^{3+} without V_O in the supercell. In this way, we confirmed that both Tb^{3+} and Tb^{4+} ions could co-exist in a real material due to a very small total energy difference between the two states (just 0.07 eV per 96-atom supercell). In the Tb^{3+} case, its complementary hole is delocalized over a whole supercell, leading to an enhanced Fermi energy occupation by O 2p states, and, thus, enhanced hole conductivity consistent with the electrical conductivity measurements from the literature [5].

Multiple configurations for the localization of two electrons from a missing O ion were treated, if the Tb and Ce ions are reduced due to the presence of oxygen vacancy. Gibbs formation energy of V_O was calculated as function of temperature and p_{O_2}. The smallest formation energy of V_O was found for the configuration with one electron localized on Tb ion and another one on a Ce ion. The corresponding formation energy is smaller by almost a factor of 4 in a comparison with an undoped system. This is a reason for high ionic conductivity of Tb-doped ceria. Nevertheless, the formation energies for different configurations considered in the present study with localization of two electrons on different number of cations range from 0.70 eV to 2.61 eV. The Ce^{3+} cation has an energy band lying in the band gap at -1.0 eV below an empty Ce 4f band suggesting that a complex of Ce^{3+} and V_O defects (Tb^{3+} are very deep states) is responsible for the emission band in the photoluminescence spectra observed in the literature [10,11].

Acknowledgments. This research was funded by the Latvian Council of Science (under the grant project lzp-2018/1-0147). Authors thank W. Chueh, J. Serra, R. Merkle, A. Popov for fruitful discussions.

References

[1] J.M. Serra, V.B. Vert, M. Betz, V.A.C. Haanappel, W.A. Meulenberg, F. Tietz, Screening of A-Substitution in the System A0.68Sr0.3Fe0.8Co0.2O3 − δ for SOFC Cathodes, J. Electrochem. Soc. 155 (2008) B207–B214. doi:10.1149/1.2818766.

[2] R. Korobko, A. Lerner, Y. Li, E. Wachtel, A.I. Frenkel, I. Lubomirsky, In-situ extended X-ray absorption fine structure study of electrostriction in Gd doped ceria, Appl. Phys. Lett. 106 (2015) 042904. doi:10.1063/1.4906857.

[3] W.C. Chueh, C. Falter, M. Abbott, D. Scipio, P. Furler, S.M. Haile, A. Steinfeld, High-Flux Solar-Driven Thermochemical Dissociation of CO_2 and H_2O Using Nonstoichiometric Ceria, Science. 330 (2010) 1797. doi:10.1126/science.1197834.

[4] M. Balaguer, C. Solís, J.M. Serra, Structural–Transport Properties Relationships on $Ce_{1-x}Ln_xO_{2-\delta}$ System (Ln = Gd, La, Tb, Pr, Eu, Er, Yb, Nd) and Effect of Cobalt Addition, J. Phys. Chem. C. 116 (2012) 7975–7982. doi:10.1021/jp211594d.

[5] M. Balaguer, C.-Y. Yoo, H.J.M. Bouwmeester, J.M. Serra, Bulk transport and oxygen surface exchange of the mixed ionic-electronic conductor $Ce_{1-x}Tb_xO_{2-\delta}$ (x = 0.1, 0.2, 0.5), J. Mater. Chem. A. 1 (2013) 10234–10242. doi:10.1039/C3TA11610G.

[6] P.A. Žguns, A.V. Ruban, N.V. Skorodumova, Ordering and phase separation in Gd-doped ceria: a combined DFT, cluster expansion and Monte Carlo study, Phys. Chem. Chem. Phys. 19 (2017) 26606–26620. doi:10.1039/C7CP04106C.
[7] D. Fuks, D. Gryaznov, E. Kotomin, A. Chesnokov, J. Maier, Dopant solubility in ceria: alloy thermodynamics combined with the DFT+U calculations, Solid State Ion. 325 (2018) 258–264. doi:10.1016/j.ssi.2018.08.019.
[8] J. Sunarso, S. Baumann, J.M. Serra, W.A. Meulenberg, S. Liu, Y.S. Lin, J.C. Diniz da Costa, Mixed ionic–electronic conducting (MIEC) ceramic-based membranes for oxygen separation, J. Memb. Sci. 320 (2008) 13–41. doi:10.1016/j.memsci.2008.03.074.
[9] H.J. Park, G.M. Choi, Oxygen permeability of gadolinium-doped ceria at high temperature, J. Eur. Ceram. Soc. 24 (2004) 1313–1317. doi:10.1016/S0955-2219(03)00555-7.
[10] J. Malleshappa, H. Nagabhushana, S.C. Sharma, D.V. Sunitha, N. Dhananjaya, C. Shivakumara, B.M. Nagabhushana, Self-propagating combustion synthesis and luminescent properties of nanocrystalline CeO2:Tb^{3+} (1–10mol%) phosphors, J. Alloys Compd. 590 (2014) 131–139. doi:10.1016/j.jallcom.2013.11.213.
[11] Z. Wang, Z. Quan, J. Lin, Remarkable Changes in the Optical Properties of CeO2 Nanocrystals Induced by Lanthanide Ions Doping, Inorg. Chem. 46 (2007) 5237–5242. doi:10.1021/ic0701256.
[12] M.L. Crespillo, J.T. Graham, F. Agulló-López, Y. Zhang, W.J. Weber, Isolated oxygen vacancies in strontium titanate shine red: Optical identification of Ti^{3+} polarons, Appl. Mater. Today. 12 (2018) 131–137. doi:10.1016/j.apmt.2018.04.006.
[13] P. Erhart, A. Klein, D. Åberg, B. Sadigh, Efficacy of the DFT + U formalism for modeling hole polarons in perovskite oxides, Phys. Rev. B. 90 (2014). doi:10.1103/PhysRevB.90.035204.
[14] R.A. Evarestov, D. Gryaznov, M. Arrigoni, E.A. Kotomin, A. Chesnokov, J. Maier, Use of site symmetry in supercell models of defective crystals: polarons in CeO_2, Phys. Chem. Chem. Phys. 19 (2017) 8340–8348. doi:10.1039/C6CP08582B.
[15] G. Kresse, D. Joubert, From ultrasoft pseudopotentials to the projector augmented-wave method, Phys. Rev. B. 59 (1999) 1758–1775. doi:10.1103/PhysRevB.59.1758.
[16] G. Kresse, J. Furthmüller, Efficiency of ab-initio total energy calculations for metals and semiconductors using a plane-wave basis set, Comput. Meter. Sci. 6 (1996) 15–50. doi:10.1016/0927-0256(96)00008-0.
[17] G. Kresse, J. Furthmüller, Efficient iterative schemes for ab initio total-energy calculations using a plane-wave basis set, Phys. Rev. B. 54 (1996) 11169–11186. doi:10.1103/PhysRevB.54.11169.
[18] J.P. Perdew, K. Burke, M. Ernzerhof, Generalized Gradient Approximation Made Simple, Phys. Rev. Lett. 77 (1996) 3865–3868. doi:10.1103/PhysRevLett.77.3865.
[19] S.L. Dudarev, D.N. Manh, A.P. Sutton, Effect of Mott-Hubbard correlations on the electronic structure and structural stability of uranium dioxide, Phil. Mag. B. 75 (1997) 613–628. doi:10.1080/13642819708202343.
[20] P.R.L. Keating, D.O. Scanlon, B.J. Morgan, N.M. Galea, G.W. Watson, Analysis of Intrinsic Defects in CeO_2 Using a Koopmans-Like GGA+U Approach, J. Phys. Chem. C. 116 (2012) 2443–2452. doi:10.1021/jp2080034.
[21] L. Shi, E. Vathonne, V. Oison, M. Freyss, R. Hayn, First-principles DFT+U investigation of charged states of defects and fission gas atoms in CeO_2, Phys. Rev. B. 94 (2016) 115132. doi:10.1103/PhysRevB.94.115132.
[22] M.B. Kanoun, A.H. Reshak, N. Kanoun-Bouayed, S. Goumri-Said, Evidence of Coulomb correction and spin–orbit coupling in rare-earth dioxides CeO_2, PrO_2 and TbO_2: An ab initio study, J. Mag. Mag. Mater. 324 (2012) 1397–1405. doi:10.1016/j.jmmm.2011.11.050.

[23] R.A. Evarestov, Quantum chemistry of solids: LCAO treatment of crystals and nanostructures, Second edition, Springer, Berlin ; New York, 2012.
[24] R.A. Evarestov, V.P. Smirnov, Supercell Model of V-Doped TiO_2: Unrestricted Hartree-Fock Calculations, Phys. Status Solidi B. 215 (1999) 949–956. doi:10.1002/(SICI)1521-3951(199910)215:2<949::AID-PSSB949>3.0.CO;2-M.
[25] R.A. Evarestov, V.P. Smirnov, Symmetry of the Model of a Crystal with a Periodic Defect: Point Defects in MgO Crystal, Phys. Status Solidi B. 201 (1997) 75–87. doi:10.1002/1521-3951(199705)201:1<75::AID-PSSB75>3.0.CO;2-3.
[26] R.A. Evarestov, A. Platonenko, D. Gryaznov, Y.F. Zhukovskii, E.A. Kotomin, First-principles calculations of oxygen interstitials in corundum: a site symmetry approach, Phys. Chem. Chem. Phys. 19 (2017) 25245–25251. doi:10.1039/C7CP04045H.
[27] R.A. Evarestov, S. Piskunov, Y.F. Zhukovskii, Site symmetry approach in the supercell model of carbon-doped ZnO bulk, Chem. Phys. Lett. 682 (2017) 91–95. doi:10.1016/j.cplett.2017.06.013.
[28] H.J. Monkhorst, J.D. Pack, Special points for Brillouin-zone integrations, Phys. Rev. B. 13 (1976) 5188–5192. doi:10.1103/PhysRevB.13.5188.
[29] M.W. Finnis, A.Y. Lozovoi, A. Alavi, The Oxidation of NiAl: What Can We Learn from Ab Initio Calculations?, Annu. Rev. Mater. 35 (2005) 167–207. doi:10.1146/annurev.matsci.35.101503.091652.
[30] J. He, R.K. Behera, M.W. Finnis, X. Li, E.C. Dickey, S.R. Phillpot, S.B. Sinnott, Prediction of high-temperature point defect formation in TiO_2 from combined ab initio and thermodynamic calculations, Acta Mater. 55 (2007) 4325–4337. doi:10.1016/j.actamat.2007.04.005.
[31] M.E. Grillo, M.W. Finnis, W. Ranke, Surface structure and water adsorption on Fe_3O_4 (111): Spin-density functional theory and on-site Coulomb interactions, Phys. Rev. B. 77 (2008). doi:10.1103/PhysRevB.77.075407.
[32] D. Gryaznov, M.W. Finnis, R.A. Evarestov, J. Maier, Oxygen vacancy formation energies in Sr-doped complex perovskites: ab initio thermodynamic study, Solid State Ion. 254 (2014) 11–16. doi:10.1016/j.ssi.2013.10.046.
[33] P. Linstrom, NIST Chemistry WebBook, NIST Standard Reference Database 69, (1997). doi:10.18434/T4D303.
[34] S. Grimme, J. Antony, S. Ehrlich, H. Krieg, A consistent and accurate ab initio parametrization of density functional dispersion correction (DFT-D) for the 94 elements H-Pu, J. Chem. Phys. 132 (2010) 154104. doi:10.1063/1.3382344.
[35] A.L. Shluger, E.A. Kotomin, L.N. Kantorovich, Quantum-chemical simulation of impurity-induced trapping of a hole: (Li) 0 centre in MgO, J. Phys. C: Solid State Phys. 19 (1986) 4183–4199. doi:10.1088/0022-3719/19/22/007.
[36] W. Traiwattanapong, A. Janotti, N. Umezawa, S. Limpijumnong, J. T-Thienprasert, P. Reunchan, Self-trapped holes in $BaTiO_3$, J. Appl. Phys. 124 (2018) 085703. doi:10.1063/1.5036750.
[37] D. Du, M.J. Wolf, K. Hermansson, P. Broqvist, Screened hybrid functionals applied to ceria: Effect of Fock exchange, Phys. Rev. B. 97 (2018). doi:10.1103/PhysRevB.97.235203.
[38] J. Graciani, A.M. Márquez, J.J. Plata, Y. Ortega, N.C. Hernández, A. Meyer, C.M. Zicovich-Wilson, J.F. Sanz, Comparative Study on the Performance of Hybrid DFT Functionals in Highly Correlated Oxides: The Case of CeO_2 and Ce_2O_3, J. Chem. Theory Comput. 7 (2011) 56–65. doi:10.1021/ct100430q.
[39] T. Zacherle, A. Schriever, R.A. De Souza, M. Martin, Ab initio analysis of the defect structure of ceria, Phys. Rev. B. 87 (2013). doi:10.1103/PhysRevB.87.134104.
[40] L. Sun, X. Huang, L. Wang, A. Janotti, Disentangling the role of small polarons and oxygen vacancies in CeO_2, Phys. Rev. B. 95 (2017). doi:10.1103/PhysRevB.95.245101.

[41] H. Jiang, P. Rinke, M. Scheffler, Electronic properties of lanthanide oxides from the G W perspective, Phys. Rev. B. 86 (2012). doi:10.1103/PhysRevB.86.125115.
[42] R.C. Karnatak, J.-M. Esteva, H. Dexpert, M. Gasgnier, P.E. Caro, L. Albert, X-ray absorption studies of CeO_2, PrO_2, and TbO_2. I. Manifestation of localized and extended f states in the 3d absorption spectra, Phys. Rev. B. 36 (1987) 1745–1749. doi:10.1103/PhysRevB.36.1745.
[43] J.J. Plata, A.M. Márquez, J.F. Sanz, Electron Mobility via Polaron Hopping in Bulk Ceria: A First-Principles Study, J. Phys. Chem. C. 117 (2013) 14502–14509. doi:10.1021/jp402594x.
[44] H.L. Tuller, A.S. Nowick, Small polaron electron transport in reduced CeO2 single crystals, J. Phys. Chem. Solids. 38 (1977) 859–867. doi:10.1016/0022-3697(77)90124-X.
[45] H.L. Tuller, Defect Structure and Electrical Properties of Nonstoichiometric CeO2 Single Crystals, J. Electrochem. Soc. 126 (1979) 209. doi:10.1149/1.2129007.
[46] B. Li, X. Huang, H. Guo, Y. Zeng, Energy transfer and tunable photoluminescence of LaBWO 6 :Tb 3+ ,Eu 3+ phosphors for near-UV white LEDs, Dyes Pigm. 150 (2018) 67–72. doi:10.1016/j.dyepig.2017.11.003.
[47] K. Momma, F. Izumi, VESTA 3 for three-dimensional visualization of crystal, volumetric and morphology data, J. Appl. Cryst. 44 (2011) 1272–1276. doi:10.1107/S0021889811038970.

Institute of Solid State Physics, University of Latvia as the Center of Excellence has received funding from the European Union's Horizon 2020 Framework Programme H2020-WIDESPREAD-01-2016-2017-TeamingPhase2 under grant agreement No. 739508, project CAMART²